www.springer.com/41230
https://doi.org/10.1007/s41230-025-4146-6
Research & Development CHINA FOUNDRY
Vol. 22 No. 3 May 2025

Effect of Al content on phase evolution, damping capacity, and mechanical properties of Al_xCrFe_3Ni medium entropy alloys

Ning-ning Geng[1], Jiang Li[1], *Wei Zhang[1, 2], Peng Gao[3], Qing-chun Xiang[1], Ying-lei Ren[1], Bo Yu[3], and **Ke-qiang Qiu[1]

1. School of Materials Science and Engineering, Shenyang University of Technology, Shenyang 110870, China

2. Key Laboratory of Light Metal Materials and Engineering at Universities of Liaoning Province, Shenyang University of Technology, Shenyang 110870, China

3. Shenyang Research Institute of Foundry Co. Ltd. CAM, Shenyang 110022, China

Abstract: The phase constitution, microstructure, damping capacity, and mechanical properties of as-cast Al_xCrFe_3Ni (x=0.5, 0.52, 0.54, and 0.56, respectively) medium entropy alloys were investigated. It is found that the volume fraction of BCC phase increases while that of FCC decreases with increasing the Al content. When the content of Al is 0.54, the alloy is composed of 82.1vol.% BCC matrix and 17.9vol.% FCC phase. Wherein the FCC phase is distributed on the BCC matrix, forming a structure where the hard BCC matrix is surrounded by soft FCC phase. This results in a hindering effect on the propagation process of vibration waves. The damping performance of $Al_{0.54}CrFe_3Ni$ alloy, characterized by an internal friction of Q^{-1} is as high as 0.059, is higher than that of most FeCr damping alloys. The volume fraction of the BCC phase and the peculiar distribution of the FCC phase are identified as the key factors affecting the damping capacity. In addition, the $Al_{0.54}CrFe_3Ni$ alloy exhibits a high yield strength of 811.16 MPa.

Keywords: medium entropy alloys; phase constitution; damping capacity; mechanical properties

CLC numbers: TG146.21 **Document code:** A **Article ID:** 1672-6421(2025)03-345-07

1 Introduction

High-entropy alloys (HEAs) have become a prominent research hotspot in material science since 2004 [1, 2] due to their superior properties such as high strength and plasticity [3, 4], good corrosion resistance [5], high thermal stability [6], good fatigue properties [7], and excellent radiation resistance [8], which have shown many potential applications in engineering. HEAs typically consist of five or more principal elements with the content of each element ranges from 5at.% to 35at.% and the entropy value greater than 1.5R (R is the gas constant). When the element number is reduced to 3 to 4 and the entropy value is reduced to 1R to 1.5R, the alloys are defined as medium entropy alloys (MEAs), which have also become a research hotspot because of their good comprehensive mechanical properties [9].

The HEAs and MEAs, generally, exhibit phase constitution in the form of face-centered cubic (FCC), body-centered cubic (BCC) or hexagonal close-packed (HCP) solid solutions or a combination thereof, rather than more complex phases [10]. It has been observed that the alloys characterized by a single FCC structure typically exhibit high plasticity albeit with diminished yield strength [11], while the alloys with a single BCC structure exhibit high strength at the expense of plasticity [12]. Leveraging the superior strength of HEAs or MEAs with a BCC phase and the enhanced plasticity of those with an FCC phase offers use inspiration for the development of damping alloys by using hard BCC structure as the matrix and soft FCC structure as the second phase. Furthermore, the inherent ferromagnetic damping effect of the hard BCC phase enhances the overall damping capacity of these alloys.

Traditional Fe-based damping alloys, e.g., Fe-Cr [13-16] and Fe-Al [17-19], are commonly used in industry to address issues related to certain kinds of vibration and

***Wei Zhang**

Ph. D., Associate Professor. He mainly engages in nonequilibrium materials and advanced cast ferrous metal materials. To date, he has published more than 40 technical papers and possesses 10 patents for invention.

****Ke-qiang Qiu**

E-mail: kqqiu@sut.edu.cn

Received: 2024-07-12; Revised: 2024-11-18; Accepted: 2025-01-22

noise, in which the Fe-Cr based alloys have been extensively studied and their highest damping capacities evaluated by measuring internal friction (Q^{-1}) at different strain amplitudes are detailed in Table 1. Additionally, Table 1 includes internal friction of various HEAs and MEAs [20-23] that contain key elements such as Fe and Cr. It is observed that the damping capacities of HEAs and MEAs generally surpass those of traditional Fe-Cr based damping alloys. For example, the microstructure of $Fe_{60}Mn_{20}Co_5Cr_{15}$ HEA, synthesized by mechanical alloying and spark plasma sintering [21], mainly consists of BCC and FCC phases. The combined effects of ferromagnetic and dislocation damping within these phases result in a damping value of 0.054. In addition, the $Al_{0.37}CrFeNi$ alloy composed of BCC matrix and FCC second phase prepared using casting method has a damping value of 0.0709 under the combined effects of ferromagnetic damping and interfacial damping [22].

Although the damping properties of HEAs and MEAs containing Fe and Cr are generally higher than those of traditional Fe-Cr damping alloys, their complex preparation methods (e.g., prepared by spark plasma sintering after mechanical alloying) or high raw material costs (e.g., high Ni content) limit their engineering applications. Therefore, it is of great scientific significance to develop HEAs or MEAs with high damping capacity by increasing the content of cheap metal elements (such as Fe) or using simple melting and casting methods. In this work, the molar number of Fe was increased from 1 to 3 based on the $Al_xCrFeNi$ alloy [22], and the microstructure, damping properties, and mechanical properties of as-cast Al_xCrFe_3Ni (x=0.5, 0.52, 0.54, and 0.56) alloys with the entropy values of 1.169R, 1.173R, 1.177R, and 1.181R, respectively, were analyzed. This work aims to enhance comprehension of the damping capacity of Fe-Cr based medium-entropy alloys with high Fe content.

Table 1: Damping capacity (Q^{-1}) of conventional Fe-Cr based alloys, HEAs, and MEAs

Fe-Cr alloys	Q^{-1}	Refs.	HEAs or MEAs	Q^{-1}	Refs.
Fe-18Cr	0.038	[13]	$FeCrMn_{0.3}VCu_{0.06}$	0.0065	[20]
Fe-13Cr-4Al-0.5Nb	0.011	[14]	$Fe_{60}Mn_{20}Co_5Cr_{15}$	0.054	[21]
Fe-13Cr-2Al-1Si	0.0072	[15]	$Al_{0.37}FeCrNi$	0.0709	[22]
Fe-16Cr-2.5Mo-0.2V	0.037	[16]	$Al_{0.25}Fe_3Cr_2NiCu$	0.056	[23]

2 Materials and methods

Alloy ingots with nominal compositions of Al_xCrFe_3Ni (x=0.5, 0.52, 0.54, and 0.56) were prepared by arc-melting bulk metal elements with purity higher than 99.9wt.% under a high-purity argon atmosphere in a water-cooled Cu crucible. The alloys were labeled as Al_x for simplicity, including $Al_{0.5}$, $Al_{0.52}$, $Al_{0.54}$, and $Al_{0.56}$, respectively. To ensure chemical uniformity, the ingots underwent five remelting cycles. Subsequently, the alloy ingots were subjected to induction heating in a quartz tube under high vacuum conditions and injected into a copper mold with internal dimensions of 70 mm×14 mm×2 mm by utilizing high-purity argon at 2 atm pressure. The vacuum of both the arc-melting and the induction melting furnaces during the preparation of the master alloy ingots and casting samples was maintained at levels below 5×10^{-3} Pa.

Samples with the dimensions of 35 mm×14 mm×2 mm used for the dynamic mechanics analyzer (DMA) were obtained via spark cutting from the original as-cast samples. The phase constitution of the as-cast samples was analyzed using a Shimadzu 7000 X-ray diffractometer (XRD) with Cu Kα radiation at a scanning rate of 4°·min^{-1}. Further examination of the phase structure was carried out with JEM-2100 transmission electron microscopy (TEM). The TEM samples, 3 mm in diameter, were made by mechanical grinding until reaching a thickness of 50 µm and were then thinned by the GATAN695 Ion Beam Thinner (IBT). Phase distributions and phase volume fractions were analyzed by electron backscatter diffraction (EBSD) with a scanning step of 1.5 µm and the sampling procedure was similar to that of TEM. The microstructure of the Al_xCrFe_3Ni alloys was observed using a GeminiSEM-300 thermal field emission scanning electron microscope (SEM), with samples prepared via electrolytic polishing in a 1:9 perchloric acid ethanol solution. Damping capacity was obtained at room temperature utilizing the TA-Q800 DMA, and it was evaluated through internal friction Q^{-1} (Q^{-1}=tanδ, where δ represents the phase lag between applied cyclic stress and strain). The DMA tests were carried out in single cantilever mode at a frequency of 1 Hz, with the strain amplitudes ranging from 1×10^{-5} to 1×10^{-3}. A universal mechanical testing machine (MTS-E45) was used to test the tensile sample at a tensile rate of 1×10^{-3} s^{-1}, and three samples for each alloy were tested in parallel to ensure the accuracy of the experiment.

3 Results and discussion

The XRD patterns of the as-cast Al_xCrFe_3Ni (x=0.5, 0.52, 0.54, and 0.56) MEAs are depicted in Fig. 1. For x values between 0.5 and 0.56, the alloy exhibits a combination of BCC and FCC phases. Notably, as the Al content increases, the intensity of the FCC peaks progressively reduces, while that of the BCC peaks steadily increases. When x=0.5, the difference of the peak intensity between the BCC phase and the FCC phase is small, which means that the matrix phase of the alloy cannot be directly determined, and it will be analyzed subsequently by EBSD. When x=0.56, the alloy mainly consists of two different BCC phases [referred to as the FeCr (BCC) phase and the AlNi (B2) phase, respectively] and a small amount of FCC phase, and the distribution and structure morphology of which will be discussed later. The increased presence of Al facilitates the formation of the BCC phase within the MEA. This is mainly attributed to the reduced valence electron number induced by Al [24].

To substantiate the phase structure, distribution, and volume fraction of the alloys, EBSD tests were conducted on the as-cast Al_x (x=0.5, 0.52, 0.54, and 0.56) MEAs, as depicted in Fig. 2. The visual analysis from Fig. 2 reveals the presence of both BCC and FCC phases in all four alloys, in which the blue and the red colors symbolize the FCC and BCC phases, respectively. The volume fractions of FCC and BCC phases in Al_x alloys are detailed in Table 2. Notably, the $Al_{0.5}$ alloy shows an almost balanced distribution with 52.9vol.% BCC phase acting as the matrix and 47.1vol.% FCC phase embedded in the matrix. As x increases to 0.52 and 0.54, as shown in Figs. 2(b) and (c), the BCC phase dominates in volume, while the FCC phase diminishes significantly. Particularly, in the $Al_{0.54}$ alloy, the FCC phase with 17.9vol.% exhibits a mesh-like structure in the BCC matrix with 82.1vol.%. The microstructure of $Al_{0.56}$ alloy shown in Fig. 2(d) predominantly comprises a BCC phase (98.3vol.%), with minimal FCC phase (1.7vol.%) in the BCC matrix, which explains that the FCC diffraction peaks can hardly be observed in the XRD pattern of the as-cast $Al_{0.56}$ alloy shown in Fig. 1. Through the EBSD analysis, the change of phase constitution as well as phase fractions of the Al_x alloys can be systematically delineated, offering insights into their distinctive microstructural features.

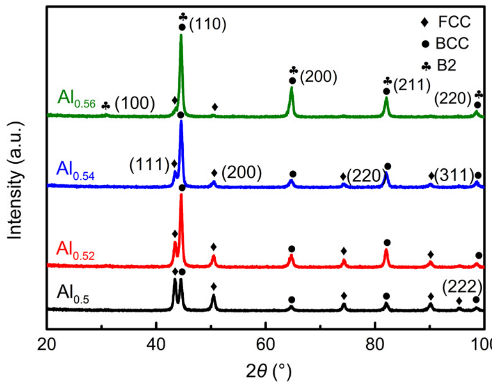

Fig. 1: XRD patterns of as-cast Al_xCrFe_3Ni (x=0.5, 0.52, 0.54, and 0.56) alloys

Figure 3 shows the morphologies of the as-cast Al_x alloys with different Al contents, and the corresponding element distribution is shown in Fig. 4. It can be intuitively seen that each alloy exhibits a different microstructure, and some elements, especially Al in $Al_{0.5}$, $Al_{0.52}$, and $Al_{0.54}$ alloys, show different degrees of segregation. For $Al_{0.5}$ alloy, as shown in Fig. 3(a) and Fig. 4(a), Ni is enriched in the spike like region while Cr is enriched in the matrix region, suggesting a coexistence of FCC and BCC phases. Combining the EBSD results, the spike like region in Fig. 3 exhibits an FCC structure, while the matrix region possesses a BCC structure. This segregation pattern arises from the simultaneous presence of FCC and BCC phases. Cr stabilizes the BCC structure, while Ni stabilizes the FCC structure, corresponding to the previous work [3]. For $Al_{0.52}$ alloy as shown in Fig. 3(b), the morphology of the FCC phase area akin to $Al_{0.5}$. When x=0.54, as shown in Fig. 3(c), the alloy displays a more uniform morphology but uneven elemental distribution. Conversely, $Al_{0.56}$ shows distinct dendrite (DR) and interdendrite (ID) structures with uniform elemental distribution, as shown in Fig. 3(d). The results indicate that the increase of Al

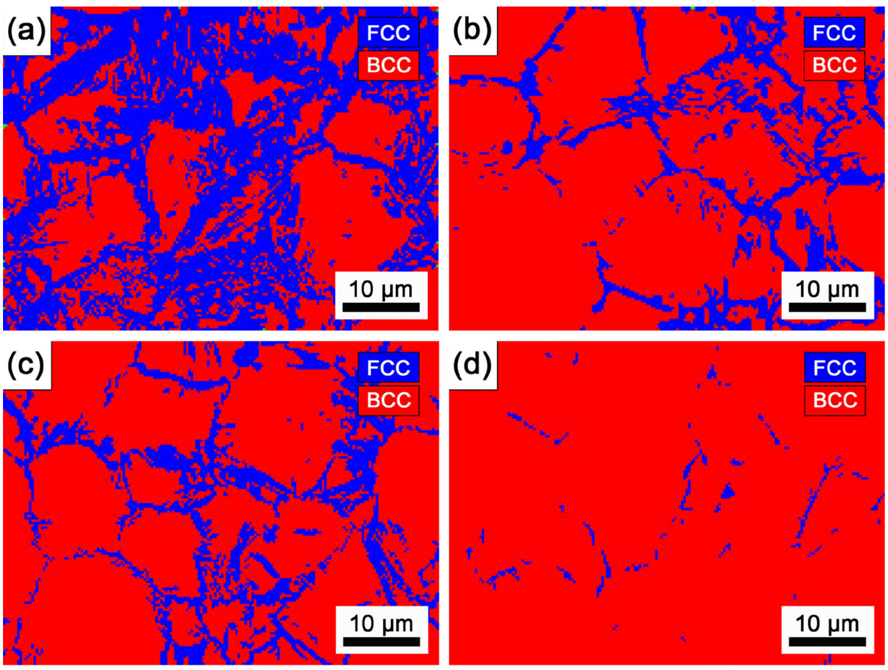

Fig. 2: EBSD maps of as-cast Al_xCrFe_3Ni (x=0.5, 0.52, 0.54, and 0.56) alloys, where (a), (b), (c), and (d) are corresponding to x=0.5, 0.52, 0.54, and 0.56, respectively

content promotes the evolution of FCC phase into BCC phase in Al_x alloys and transforms disordered BCC into ordered B2 phase, corroborating prior research findings [25]. These results underscore the microstructural variations and phase transformations influenced by Al content in the Al_x alloys.

Table 2: Volume fractions of BCC and FCC phases in as-cast Al_xCrFe_3Ni alloys

Alloys	BCC (vol.%)	FCC (vol.%)
$Al_{0.5}$	52.9	47.1
$Al_{0.52}$	79.7	20.3
$Al_{0.54}$	82.1	17.9
$Al_{0.56}$	98.3	1.7

To identify the phase structure and microstructure of the BCC and FCC phases in the Al_x alloys, TEM analysis was conducted. Figure 5 exhibits bright field images and corresponding selected area electron diffraction (SAED) patterns for the Al_x alloys. In the TEM image of the $Al_{0.5}$ alloy, as shown in Fig. 5(a), the phase distribution reveals dark strips (represented by blue squares) alongside bright strips (represented by red squares). The corresponding SAED patterns confirm that the dark strip has an FCC structure, while the bright strip exhibits a BCC structure, as shown in Fig. 5(a). The microstructures of $Al_{0.52}$, $Al_{0.54}$, and $Al_{0.56}$ alloys demonstrate a predominant BCC phase (red square) and FCC phase (blue square) akin to the $Al_{0.5}$ alloy. Notably, small spherical precipitates are observed in the BCC phase regions of the alloys, while absent in the FCC phases. To determine the structure of the spherical precipitates, a dark field analysis

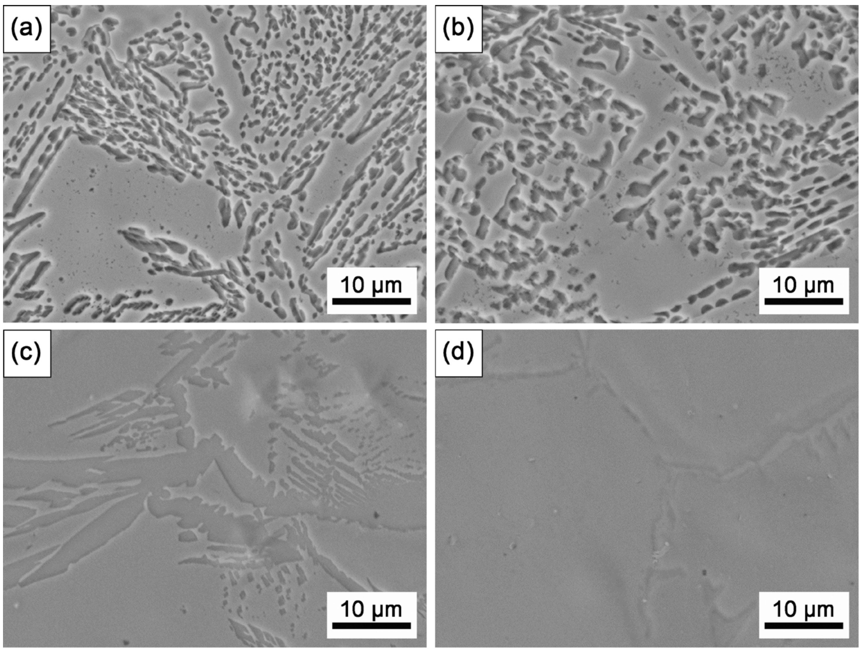

Fig. 3: SEM images of as-cast $Al_{0.5}$ (a), $Al_{0.52}$ (b), $Al_{0.54}$ (c), and $Al_{0.56}$ (d) alloys

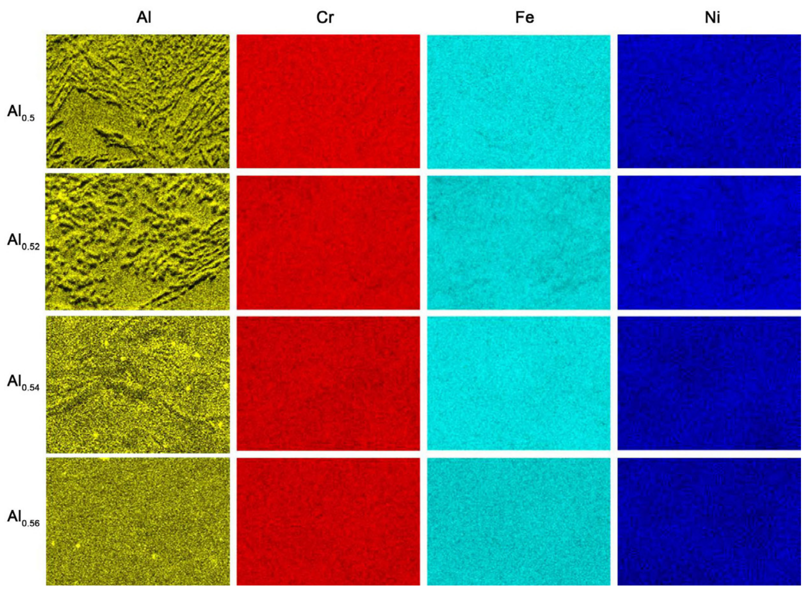

Fig. 4: EDS results of the distribution of Al, Cr, Fe, and Ni elements in Al_x alloys

of its BCC phase region was performed [represented by white squares in Fig. 5(c)]. The labeled regions (I and II) of the $Al_{0.54}$ alloy were chemically analyzed using a TEM equipped with an energy spectrometer, and the corresponding elemental compositions of Al, Cr, Fe, and Ni are (5.82at.%, 29.82at.%), (31.55at.%, 8.28at.%), (54.16at.%, 19.98at.%), and (8.47at.%, 41.92at.%) for Regions I and II, respectively. This indicates that Fe and Cr elements corresponding to the BCC phase are enriched in Region I, while Ni and Al elements corresponding to the B2 phase are enriched in Region II. Meanwhile, the average diameters of the B2 phase in $Al_{0.52}$, $Al_{0.54}$, and $Al_{0.56}$ alloys corresponding to 35.654, 73.065, and 60.354 nm, respectively, were counted using image pro plus software.

The tensile stress-strain curves of the Al_x alloys are illustrated in Fig. 6, showing an upward trend in yield strengths with increasing Al content. The measured yield strengths are 564.80 MPa, 767.55 MPa, 811.16 MPa, and 915.45 MPa for the $Al_{0.5}$, $Al_{0.52}$, $Al_{0.54}$, and $Al_{0.56}$ alloys, respectively. The ultimate tensile strength of the Al_x alloys shows the same trend as the yield strength. However, the plastic strain of the alloys becomes progressively smaller with increasing Al content, decreasing from 16.63% for the $Al_{0.5}$ alloy to 2.99% for the $Al_{0.56}$ alloy. Typically, BCC phases are higher strength but less ductile, while FCC phases offer greater ductility but lower strength. Hence, for the studied alloys, the increase in BCC volume fraction caused by the increase of Al content contributes to the enhanced strength and leads to the reduce of plasticity, highlighting the well recognized relationship between phase constitution and mechanical properties [26]. The morphologies of tensile fracture surface of the Al_x (x=0.5, 0.52, 0.54, and 0.56) alloys are shown in Fig. 7. As can be seen from Fig. 7, the fracture surface of the $Al_{0.5}$ alloy is almost entirely filled with dimples. In addition to a large number of dimples, there are several pits on the fracture surface of $Al_{0.52}$ alloy. With further increasing the Al content, the fracture surface of $Al_{0.54}$ and $Al_{0.56}$ alloys begin to appear obvious cleavage face. This phenomenon mainly results from the increased volume fraction of BCC phase caused by the increase of Al content.

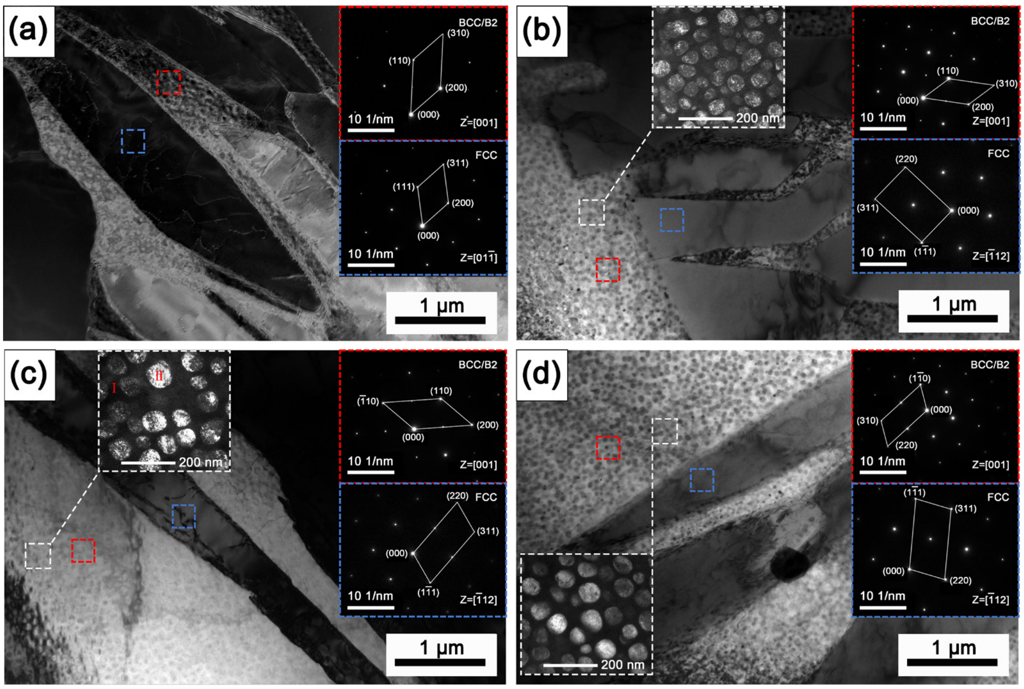

Fig. 5: TEM images and corresponding SAED patterns of $Al_{0.5}$ (a), $Al_{0.52}$ (b), $Al_{0.54}$ (c), and $Al_{0.56}$ (d) alloys

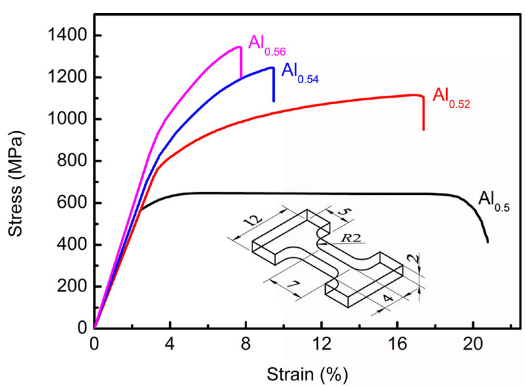

Fig. 6: Tensile stress-strain curves of as-cast Al_xCrFe_3Ni (x=0.5, 0.52, 0.54, and 0.56) alloys measured at room temperature

The plots in Fig. 8 illustrate the relationship between internal friction Q^{-1} and strain amplitude γ at 1 Hz for the as-cast Al_x (x=0.5, 0.52, 0.54, and 0.56) alloys. Notably, the Q^{-1} values for these alloys exhibit a rapid initial increase, particularly pronounced in higher Al content alloys. The Q^{-1} then reaches a maximum value and the curves eventually level off or decline. The maximum damping capacities for $Al_{0.5}$ to $Al_{0.56}$ alloys are 0.05405, 0.05132, 0.05919, and 0.05222, respectively. The $Al_{0.54}$ alloy, featuring a BCC matrix and 17.9vol.% FCC secondary phase, displays the highest damping properties, having a peak Q^{-1} value of 0.05919.

The damping capacity is inherently linked to the phase constitution, where an increase in Al content corresponds to an increase in BCC phase and a decrease in FCC phase.

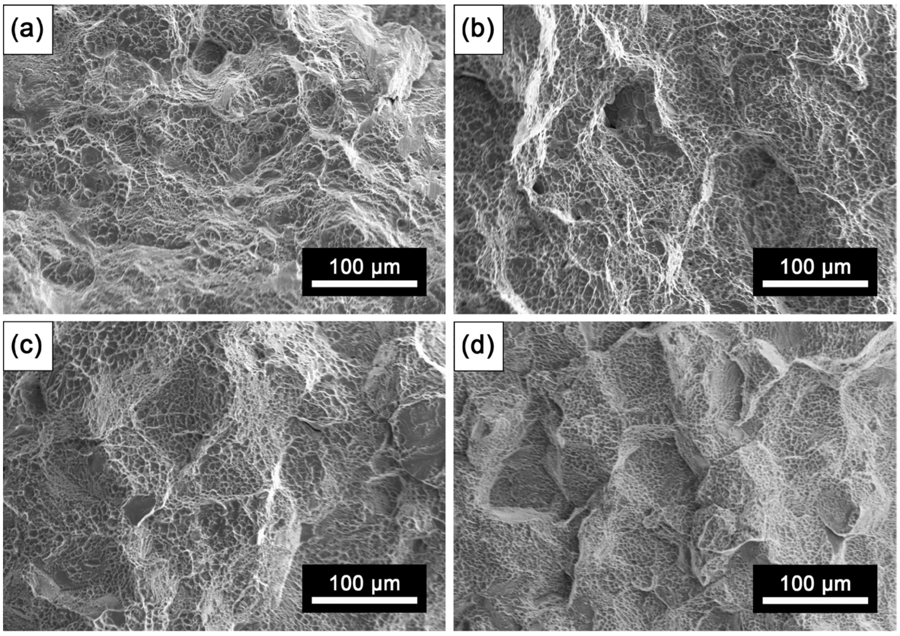

Fig. 7: Tensile fracture surfaces of as-cast Al_xCrFe_3Ni alloys, where (a), (b), (c), and (d) corresponding to x=0.5, 0.52, 0.54, and 0.56, respectively

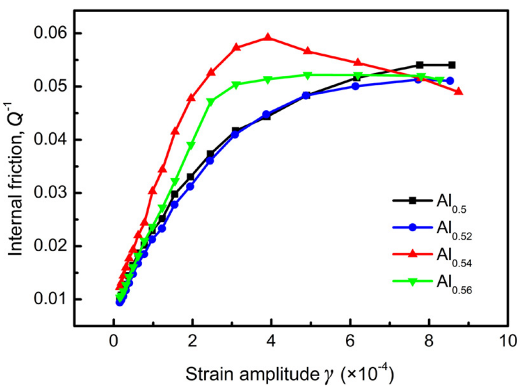

Fig. 8: Damping capacity-strain amplitude curves of as-cast Al_xCrFe_3Ni alloys

This relationship between phase constitution and damping behavior underscores the multifaceted interplay between alloy microstructure and damping properties, which can be expressed as [27]:

$$Q^{-1} = \frac{4KE^2\lambda\gamma}{3\pi\sigma_i} \tag{1}$$

where K is a non-dimensional constant, E is the Young's modulus, λ is the magnetostrictive coefficient, γ is the strain amplitude, and σ_i is the average internal stress. The damping properties of alloys are closely related to their phase constitution, particularly the magnetostriction coefficient, λ, which influences the internal friction, Q^{-1}. The equation reveals a proportional relationship between Q^{-1} and λ, emphasizing the impact of magnetic phase on damping behavior. It is known that the BCC phase with a higher Fe content (i.e., it contains ferromagnetic elements in its composition) has better ferromagnetic damping [28], that is, the alloys containing a higher volume fraction of the BCC phase demonstrate larger λ values and consequently higher Q^{-1} values. Namely, alloys rich in BCC phases tend to outperform than those with lower BCC content in terms of damping. This highlights the significant role of the ferromagnetic damping mechanism attributed to the BCC matrix. Interestingly, the volume fraction of BCC phase is the highest in $Al_{0.56}$ alloy and second highest in $Al_{0.54}$ alloy, while the value of Q^{-1} for $Al_{0.54}$ alloy is higher than that of the $Al_{0.56}$ alloy. This discrepancy suggests that the interfacial damping within the alloy also plays a pivotal role in influencing damping properties, manifesting the intricate interplay between internal structure and damping dynamics within the Al_x alloys, which follows the equation [23]:

$$Q^{-1} = \frac{4.5(1-\nu)}{\pi^2(2-\nu)} V_{\mathrm{p}} \tag{2}$$

where ν is the Poisson's ratio, and V_{p} is the volume fraction of the second phase. The evaluation of damping capacity in alloys entails various factors, including the Poisson's ratio and the volume fraction of the second phase. The Q^{-1} value of an alloy is directly proportional to the second phase volume fraction, i.e., the higher the V_{p}, the higher the Q^{-1} value. For instance, the $Al_{0.54}$ alloy possessing 17.9vol.% FCC second phase outperforms the $Al_{0.56}$ alloy with only 1.7vol.% FCC phase. Especially, the soft FCC phase in $Al_{0.54}$ alloy is distributed in the hard BCC matrix with a mesh-like structure, as shown in Fig. 2, which results in the hindering effect on the propagation of vibration waves. Therefore, under the combined effect of ferromagnetic damping and interfacial damping, the $Al_{0.54}$ alloy has the highest damping capability. The experimental alloys in this work, harnessing diverse damping mechanisms, including ferromagnetic and interfacial damping, show a peak value of damping capacity (Q^{-1}) higher than that of traditional FeCr damping alloys, demonstrating a blend of exceptional damping capacities and robust mechanical properties.

4 Conclusions

(1) With increasing Al content in Al_xCrFe_3Ni (x=0.5, 0.52, 0.54, and 0.56) alloys, the volume fraction of BCC phase increases, which enhances both the yield and fracture strengths of the alloys, indicating the pivotal role of phase constitution. The volume fraction of BCC phase in the Al_xCrFe_3Ni alloys increases from 52.9% to 98.3% as x increases from 0.5 to 0.56, resulting in an increase in the yield strength of the alloy from 564.80 MPa to 915.45 MPa.

(2) Both the ferromagnetic damping and interfacial damping affect the damping capacity of Al_xCrFe_3Ni alloys. The $Al_{0.54}$ alloy, featuring 82.1vol.% hard BCC phase as matrix and 17.9vol.% mesh-like FCC phase distributed on the matrix, demonstrates the highest damping capacity of 0.05919 at a frequency of 1 Hz and a strain amplitude of 3.9×10^{-4}.

Acknowledgment

This work was supported by the Natural Science Foundation of Liaoning Province (No. 2022-BS-181).

Conflict of interest

Prof. Qing-chun Xiang is an EBM of *CHINA FOUNDRY*. He was not involved in the peer-review or handling of the manuscript. The authors have no other competing interests to disclose.

References

[1] Yeh J W, Chen S K, Lin S J, et al. Nanostructured high-entropy alloys with multiple principal elements: Novel alloy design concepts and outcomes. Advanced Engineering Materials, 2004, 6(5): 299–303.

[2] Cantor B, Chang I T H, Knight P, et al. Microstructural development in equiatomic multicomponent alloys. Materials Science and Engineering: A, 2004, 375: 213–218.

[3] Zhang T, Zhao R D, Wu F F, et al. Transformation-enhanced strength and ductility in a FeCoCrNiMn dual phase high-entropy alloy. Materials Science and Engineering: A, 2020, 780: 139182.

[4] Acciarri M D, La Roca P, Guerrero L M, et al. Effect of FCC anti-ferromagnetic ordering on the stability of phases in $Fe_{60-x}Mn_{30}Cr_{10}Co_x$ high entropy alloys. Journal of Alloys and Compounds, 2020, 823: 153845.

[5] Thapliyal S, Nene S S, Agrawal P, et al. Damage-tolerant, corrosion-resistant high entropy alloy with high strength and ductility by laser powder bed fusion additive manufacturing. Additive Manufacturing, 2020, 36: 101455.

[6] Deng H W, Xie Z M, Wang M M, et al. A nanocrystalline AlCoCuNi medium-entropy alloy with high thermal stability via entropy and boundary engineering. Materials Science and Engineering: A, 2020, 774: 138925.

[7] Li W, Chen S, Liaw P K. Discovery and design of fatigue-resistant high-entropy alloys. Scripta Materialia, 2020, 187(12): 68–75.

[8] Cao P P, Wang H, He J Y, et al. Effects of nanosized precipitates on irradiation behavior of CoCrFeNi high entropy alloys. Journal of Alloys and Compounds, 2020, 859: 158291.

[9] Moon J, Park J M, Bae J W, et al. A new strategy for designing immiscible medium-entropy alloys with excellent tensile properties. Acta Materialia, 2020, 193: 71–82.

[10] Zhuang Y X, Zhang X L, Gu X Y. Effect of annealing on microstructure and mechanical properties of $Al_{0.5}CoCrFeMo_xNi$ high-entropy alloys. Entropy, 2018, 20(11): 812.

[11] Ye Q, Yang G, Yang B. Effect of aging on microstructure and property of $AlCoCrFeMo_{0.05}Ni_2$ high entropy alloy. Materials Science and Engineering: A, 2019, 760: 1–6.

[12] Tang Z, Zhang S, Cai R, et al. Designing high entropy alloys with dual fcc and bcc solid-solution phases: Structures and mechanical properties. Metallurgical and Materials Transactions: A, 2019, 50: 1888–1901.

[13] Mohamed A K, Zadorozhnyy M Y, Saveliev D V, et al. Damping capacity, magnetic and mechanical properties of Fe-18Cr alloy. Journal of Magnetism and Magnetic Materials, 2020, 494: 165777.

[14] Wang H, Wang F, Liu H, et al. Influence of alloy elements (Mo, Nb, Ti) on the strength and damping capacity of Fe-Cr based alloy. Materials Science and Engineering: A, 2016, 667: 326–331.

[15] Wang H, Li W, Hao T, et al. Mechanical property and damping capacity of ultrafine-grained Fe-13Cr-2Al-1Si alloy produced by equal channel angular pressing. Materials Science and Engineering: A, 2017, 695: 193–198.

[16] Xu X Q, Xu Y. Higher damping capacity induced by negative magnetostriction of Fe-16Cr-2.5Mo-0~0.2V alloys. Journal of Alloys and Compounds, 2021, 852: 156673.

[17] Smith D A, Rai A, Lim Y, et al. Magnetic damping in epitaxial iron alloyed with vanadium and aluminum. Physical Review Applied, 2020, 14(3): 034042.

[18] Chang H W, Jen S U, Tseng D H, et al. Magneto-mechanical properties of $Fe_{100-x}Al_x$ alloys (x=14–27) prepared by directional solidification. Journal of Alloys and Compounds, 2020, 844: 156086.

[19] Lambri O A, Weidenfeller B, Bonifacich F G, et al. Damping of Fe-Al alloy electrodeposited in an ionic liquid. Materials Research, 2018, 21: e20170805.

[20] Song R K, Ye F, Yang C X, et al. Effect of alloying elements on microstructure, mechanical and damping properties of Cr-Mn-Fe-V-Cu high-entropy alloys. Journal of Materials Science & Technology, 2018, 34: 2014–2021.

[21] Chen Q, Zhang H, Zhou S, et al. A novel high-entropy alloy with excellent damping property toward a large strain amplitude environment. Journal of Alloys and Compounds, 2019, 802: 493–501.

[22] Wang H, Zhang W, Gao P, et al. $Al_xCrFeNi$ medium entropy alloys with high damping capacity. Journal of Alloys and Compounds, 2021, 876: 159991.

[23] Han X N, Li Q F, Wang H D, et al. Damping capacity and mechanical properties of $Fe_3Cr_2NiCuAl_x$ medium entropy alloys by tuning phase constituents. Journal of Alloys and Compounds, 2022, 910: 164884.

[24] Wang C, Tracy C L, Park S, et al. Phase transformations of Al-bearing high-entropy alloys $Al_xCoCrFeNi$ (x=0, 0.1, 0.3, 0.75, 1.5) at high pressure. Applied Physics Letter, 2019, 114(9): 091902.

[25] Stepanov N D, Shaysultanov D G, Chernichenko R S, et al. Effect of Al on structure and mechanical properties of Fe-Mn-Cr-Ni-Al non-equiatomic high entropy alloys with high Fe content. Journal of Alloys and Compounds, 2019, 770: 194–203.

[26] Huang H, Wu Y, He J, et al. Phase-transformation ductilization of brittle high-entropy alloys via metastability engineering. Advanced Materials, 2017, 29(30): 1701678.

[27] Duan L, Pan D, Wang H, et al. Investigation of the effect of alloying elements on damping capacity and magnetic domain structure of Fe-Cr-Al based vibration damping alloys. Journal of Alloys and Compounds, 2017, 695: 1547–1554.

[28] Smith G W, Birchak J R. Internal stress distribution theory of magnetomechanical hysteresis–An extension to include effects of magnetic field and applied stress. Journal of Applied Physics, 1969, 40(13): 5174–5178.